Journal of Materials Chemistry C

View Article Online
View Journal | View Issue

Pb(Fe$_{0.5}$Nb$_{0.5}$)O$_3$–BiFeO$_3$-based multicalorics with room-temperature ferroic anomalies†

Uroš Prah, [ID] *[ab] Magdalena Wencka,[c] Tadej Rojac,[ab] Andreja Benčan[ab] and Hana Uršič [ID] [ab]

The search for new single-phase multicaloric materials, combining electrocaloric and magnetocaloric effects, is just at its beginning. Since the highest caloric effects are obtained near ferroic phase transitions, multiferroics with room-temperature ferroic anomalies are promising candidates for multicaloric cooling. In this work, such materials were prepared by tailoring the temperature of the ferroic anomalies by introducing BiFeO$_3$, a material possessing high-temperature ferroic phase transitions, into the multicaloric Pb(Fe$_{0.5}$Nb$_{0.5}$)O$_3$ to form a solid solution. A series of (1−x)Pb(Fe$_{0.5}$Nb$_{0.5}$)O$_3$−xBiFeO$_3$ (x = 0–0.5) were prepared. Among them, 0.8Pb(Fe$_{0.5}$Nb$_{0.5}$)O$_3$−0.2BiFeO$_3$ exhibits both dielectric permittivity and magnetic susceptibility anomalies at room temperature and is therefore one of the first such single-phase materials. However, at higher temperatures the material exhibits excessive Joule heating that critically degrades the electrocaloric cooling effect, while the antiferromagnetic nature of the material results in a low magnetocaloric response. Because of that, the multicaloric properties of 0.8Pb(Fe$_{0.5}$Nb$_{0.5}$)O$_3$−0.2BiFeO$_3$ were further improved by doping the material with Mn and Gd ions. This results in a composition with negligible Joule heating up to 75 °C and with room-temperature electrocaloric effect of more than 1 °C, and a high magnetocaloric effect of ∼3 °C at cryogenic temperatures. Furthermore, this material also exhibits the highest room-temperature magnetocaloric effect (∼8 × 10^{-3} °C) among all already known Pb(Fe$_{0.5}$Nb$_{0.5}$)O$_3$-based multicalorics.

I. Introduction

Multiferroics are a class of materials, where in general more than one ferroic (including relaxor), antiferroic or ferric orders coexist.[1,2] A lot of attention is paid to the so-called single-phase magnetoelectric multiferroics, combining ferroelectric and ferromagnetic properties in the same material, which are attractive due to the different origins and opposite mechanisms of both ferroic orders.[2–5] Magnetoelectric multiferroics are promising candidates for future environmental friendly solid-state cooling based on the caloric effect,[6–9] which refers to the reversible adiabatic temperature changes of the material under the influence of external stimuli, such as electric or magnetic fields.[9–11]

Electrocaloric (EC) and magnetocaloric (MC) materials show drawbacks that limit their cooling capacity and consequently prevent their commercial use.[6,8] An interesting idea for improving their cooling capacity is to prepare a material that combines both EC and MC effects, hereafter called the multicaloric material.[11–13] The highest caloric effects are obtained near ferroic phase transitions, where the order parameters (*i.e.*, polarization and magnetization) are strongly temperature dependent.[11,14,15] The majority of commercially used cooling devices operate at room temperature (RT), and therefore multiferroics with broad room-temperature ferroic anomalies are promising candidates for efficient multicalorics.[14,16] However, the vast majority of them exhibit anomalies at different temperature regions, therefore, the search for single-phase multiferroics exhibiting both ferroic anomalies at RT is just at its beginning.[3,4]

The topic of multicaloric (EC + MC) materials is relatively new.[13,17–21] In 2016, the coexistence of EC and MC effects was experimentally confirmed in 0.8Pb(Fe$_{0.5}$Nb$_{0.5}$)O$_3$−0.2Pb(Mg$_{0.5}$W$_{0.5}$)O$_3$ relaxor ceramics.[22] However, this material exhibits very low EC and MC effects (both ∼0.25 °C) with the maximum values far below RT. Recently, in our previous work, careful control of sintering conditions and doping with manganese resulted in improved EC and MC properties of Pb(Fe$_{0.5}$Nb$_{0.5}$)O$_3$ (PFN) ceramics with the maximal values of 2.47 °C (at 80 °C and 140 kV cm^{-1}) and 0.44 °C (at −271 °C and 50 kOe), respectively.[23] Despite a relatively large EC effect at RT (1.59 °C at 140 kV cm^{-1}), the highest MC effect in this material is located at temperatures far below the desired RT.

^{a} *Jožef Stefan Institute, Jamova cesta 39, 1000 Ljubljana, Slovenia.*
  E-mail: uros.prah@ijs.si

^{b} *Jožef Stefan International Postgraduate School, Jamova cesta 39, 1000 Ljubljana, Slovenia*

^{c} *Institute of Molecular Physics, Polish Academy of Sciences, ul. Smoluchowskiego 17, 61-179 Poznań, Poland*

† Electronic supplementary information (ESI) available: online Supplementary material. See DOI: 10.1039/d0tc02329a

11282 | *J. Mater. Chem. C*, 2020, 8, 11282–11291

This journal is © The Royal Society of Chemistry 2020

PFN is a well-known complex perovskite, whose multiferroic behavior arises from ferroelectrically active Nb^{5+} (empty d-orbitals) and magnetically active Fe^{3+} ions (partially filled d-orbitals) that are randomly distributed in the B-site of the perovskite lattice. PFN exhibits paraelectric-to-ferroelectric phase transition (Curie temperature, T_C) at ~100 °C[23,24] and paramagnetic-to-antiferromagnetic phase transition (Néel temperature, T_N) at ~−120 °C.[23,25] At temperatures below −250 °C, an additional magnetic phase transition from long-range antiferromagnetic to short-range spin-glass-like magnetic order is present.[25,26] Because PFN already exhibited the paraelectric-to-ferroelectric phase transition together with high EC effects slightly above desired RT, it seems a promising starting point for designing multiferroic materials with room-temperature ferroic phase transitions. An idea to modify the PFN in order to shift its paramagnetic-to-antiferromagnetic phase transition (−120 °C) closer to RT is to mix PFN with $BiFeO_3$ (BFO) and form a solid solution. BFO is a well-known multiferroic material, which exhibits a paramagnetic-to-antiferromagnetic phase transition at 370 °C,[27] therefore adding BFO to PFN should ideally move the T_N of the material towards RT.

In general, BFO exhibits high specific electrical conductivity that typically occurs in the range of 10^{-10}–10^{-2} Ω^{-1} m^{-1},[27,28] while PFN is less conductive ($\sim 10^{-12}$ Ω^{-1} m^{-1}).[23] Consequently, the increasing BFO content in PFN–BFO solid solution will increase the electrical conductivity of the material, leading to the appearance of the Joule heating effect and thus lowering of the EC cooling efficiency.[29–31] According to reports on PFN[23,32] as well as BFO-based materials,[33,34] the excessive electrical conductivity can be suppressed by the addition of small amounts of Mn ions. In our previous work it was shown that adding 0.5 mol% of Mn ions efficiently suppresses the electrical conductivity of PFN.[23] Another drawback of using PFN and BFO as multicalorics is their antiferromagnetic order that leads to low magnetization, namely <0.4 emu g^{-1} at magnetic fields of 60 kOe in BFO.[35] According to the literature, in BFO, breaking the antiferromagnetic ordering and increasing the magnetic susceptibility can be achieved by the substitution of A-site of the crystal lattice with rare earth elements, such as Gd ions.[36–39] Rare earth elements possess strong localized magnetic moments that arise from the partially filled 4f inner electron shell, making them promising candidates for enhancing the magnetic properties of the materials.[40] In previous Gd-doped BFO studies,[36–39] it was shown that the addition of 12 mol% of Gd ions enhances the ferromagnetic properties and at the same time does not increase the electrical conductivity and does not lead to the formation of a non-polar phase.[37,41] However, no studies on doping of PFN–BFO have been reported, and therefore in this work, a similar approach as reported for pure PFN and BFO, namely doping with 0.5 mol% of Mn and 12 mol% of Gd ions, is employed.

In this work, seven different multiferroic $(1-x)Pb(Fe_{0.5}Nb_{0.5})O_3$–$xBiFeO_3$ (x = 0–0.5) solid solutions were prepared. Among them, PFN–20BFO exhibits both dielectric permittivity and magnetic susceptibility anomalies close to RT and is therefore a promising candidate for multicalorics. Further doping of PFN–20BFO with 0.5 mol% of Mn and 12 mol% of Gd ions

suppresses the electrical conductivity and enhances the magnetic ordering leading to the improvement of the EC and MC properties. The results of this study show the importance of composition–caloric-property inter-correlations in PFN–BFO-based ceramics.

II. Experimental

Material synthesis

PFN–$100x$BFO (x = 0, 0.05, 0.1, 0.2, 0.3, 0.4 and 0.5) ceramic powders were prepared by mechanochemical-activation-assisted synthesis using PbO (99.9%, Alfa Aesar), Fe_2O_3 (99.9%, Alfa Aesar), Nb_2O_5 (99.9%, Sigma Aldrich) and Bi_2O_3 (99.999%, Alfa Aesar) as starting oxides. The preparation process of unmodified PFN–$100x$BFO powders is described in detail in our previous work.[23,42] The same synthesis procedure was employed also for Mn-doped PFN–20BFO, where 0.5 mol% of Mn in the form of MnO_2 (99.9%, Alfa Aesar) were added to the mixture of initial oxides as a substitution for B-site cations (Fe^{3+} and Nb^{5+}) according to the nominal formula $0.8Pb(Fe_{0.5}Nb_{0.5})_{0.995}Mn_{0.005}O_3$–$0.2BiFe_{0.995}Mn_{0.005}O_3$. MnO_2 was pre-milled in an attrition mill (Netzsch, PE075/PR01, Selb, Germany) with absolute ethanol at 600 min^{-1} for 5 h using yttria-stabilized zirconia (YSZ) milling balls (ball diameter, 3 mm).

The composition with 0.5 mol% of Mn (substitution for B-site cations, Fe^{3+} and Nb^{5+}) and 12 mol% of Gd (substitution for Bi^{3+}) was prepared according to the nominal formula $0.8Pb(Fe_{0.5}Nb_{0.5})_{0.995}Mn_{0.005}O_3$–$0.2Bi_{0.88}Gd_{0.12}Fe_{0.995}Mn_{0.005}O_3$. Due to the problems with aggregation and dispersion of Gd_2O_3, for the preparation of Gd and Mn co-doped PFN–20BFO, in all starting oxides, surfactant ammonium polyacrylate (PAA) was used. The PAA, used as a steric stabilizer, was formed by mixing poly(acrylic acid) (50 wt% solution in H_2O, Sigma Aldrich) and 1-butylamine (99%, Alfa Aesar) in absolute ethanol.[43,44] Gd_2O_3 (99.99%, Metall) was pre-milled in a planetary ball mill (Retsch PM400, Retsch, Haan, Germany) at 150 min^{-1} for 4 h in an ethanol/PAA mixture using YSZ milling balls (ball diameters 3 mm). PAA was added also to all other pre-milled starting oxides and the mixtures were homogenized by milling in a planetary ball mill at 150 min^{-1} for 2 h using YSZ milling balls (ball diameter, 3 mm). A stoichiometric mixture of all starting oxides (40 g) was homogenized in a planetary ball mill at 150 min^{-1} for 4 h in absolute ethanol using YSZ milling balls (ball diameter, 3 mm). The homogenized mixture was dried and heat-treated at 350 °C for 30 min (heating and cooling rates of 2 °C min^{-1}) in order to remove PAA from the powder. The powder mixture was mechanochemically activated in the same planetary ball mill for 14 h at 400 min^{-1} in a tungsten carbide milling vial (volume 80 cm^3), filled with 7 tungsten carbide milling balls (ball diameter, 15 mm). After activation, the synthesized powder, i.e., mixtures of crystalline perovskite and amorphous phases, was re-milled in a planetary ball mill in absolute ethanol, at 200 min^{-1}, for 4 h, using YSZ milling balls (ball diameter, 3 mm).

All prepared powders were uniaxially pressed (50 MPa) into pellets of a diameter of 8 mm followed by isostatic pressing at

This journal is © The Royal Society of Chemistry 2020

J. Mater. Chem. C, 2020, **8**, 11282–11291 | **11283**

300 MPa. The powder compacts were reactively sintered in double alumina crucibles in the presence of PFN packing powder. Sintering temperatures for each composition were estimated from sintering curves (details in ref. 42). To maintain similar grain sizes, PFN–100xBFO samples with a lower content of BFO ($x \leq 0.1$) were sintered at 950 °C for 2 h, while samples with a higher content of BFO ($x \geq 0.2$) were sintered at 900 °C for 2 h. Similar thermal treatment was performed also for Mn-doped PFN–20BFO (900 °C for 2 h), while in the Mn,Gd co-doped sample, due to the different sintering behavior, a higher sintering temperature (1000 °C for 2 h) was used (shown in ESI,† A). Sintering runs were performed under an oxygen atmosphere as suggested in ref. 45 and used in our previous work.[23,42] The use of the saturated oxygen atmosphere during the sintering prevents (or minimizes) the reduction of Fe^{3+} to Fe^{2+} and reduces the amount of oxygen vacancies, which consequently resulted in a lower electrical conductivity and dielectric losses of the material.[45] For all samples, a heating and cooling rate of 2 °C min^{-1} was used.

Characterization

The densities of the sintered pellets were determined using a gas-displacement density analyzer (Micromeritics, AcuuPyc II 1340 Pycnometer) at RT. For the calculation of the relative density, the crystallographic densities were obtained from Rietveld refinement analysis (details in the ESI,† B). X-ray powder diffraction (XRD) patterns of crushed ceramic pellets were recorded on a X'Pert Pro (PANalytical B.V., Netherlands) high-resolution powder diffractometer equipped with Cu Kα_1 radiation (45 kV, 40 mA), in reflection mode. Diffraction patterns were recorded in the 10–70° 2θ-range with a step size of 0.017° and an integration time of 100 s per step at RT. The phase identification was performed with the PDF-4+ database.

The microstructure of sintered ceramics was examined using a field-emission scanning electron microscope (FE-SEM, JSM-7600F, Jeol Ltd, Japan) equipped with an energy dispersive X-ray spectrometer (EDXS, Inca Oxford 350 EDS SSD, Oxford Instruments, Abingdon, UK). Prior to microstructural analysis, the samples were fractured for fracture-surface examination, ground and fine-polished using a colloidal silica suspension, followed by thermal etching at 775 °C for 15 minutes in the presence of PFN packing powder. The average grain size and grain-size distribution were evaluated from the digitized images of etched surfaces, processed using the Image Tool software (UTHSCSA Image Tool Version 3.00. 2002)[46] by measuring more than 500 grains. The grain size is expressed as the Feret's diameter.[47]

For characterization of electrical properties, the ceramic pellets were cut, thinned and polished to a thickness of $\sim$200 μm. In order to release the internal stresses produced during the mechanical processing, the thinned ceramic pellets were heated up to 600 °C for 1 h (with 5 °C min^{-1} heating rate) and then slowly cooled down (1 °C min^{-1}) to RT. The surfaces of the pellets were coated with Au electrodes (diameter of 5 mm) using a RF-magnetron sputtering machine (5Pascal, Italy).

The relative dielectric permittivity (ε) and dielectric loss (tan δ) as a function of temperature were analyzed during cooling from 200 °C to −50 °C using an Aixacct TF analyzer

2000 (aixACCT Systems GmbH, Aachen, Germany) coupled with a HP 4284A Precision LCR impedance meter (Hewlett-Packard, California, USA) in the frequency range of 0.1–100 kHz. The DC current-density–electric-field (j–E) response was measured using a Keithley 237 (Keithley Instruments, Ohio, USA) high voltage source measuring unit. For the j–E measurements, the samples were exposed to step-like voltages within the range of ±0.5 kV cm^{-1}. In this range, from negative to positive polarity, 13 equal field steps were applied. Upon each of these steps, the voltage was maintained constant for 1.5 h for the current to stabilize, before being recorded. The specific DC electrical conductivity (σ_{DC}) was obtained from the slope assuming Ohm's law. AC current density–electric field (j–E) loops were measured at RT using an Aixacct TF analyzer 2000 by applying a single sinusoidal waveform with a frequency of 1 Hz and electric fields up to 80 kV cm^{-1}. Polarization–electric field (P–E) loops were automatically obtained with software using numerical integration of the current signal.

The EC effect was measured using the direct method. The measurements were performed on $\sim$80 μm-thick ceramic samples with sputtered Au electrodes. The direct EC measurements were performed using a modified differential scanning calorimeter (Netzsch DSC 204 F1, Selb, Germany), which allowed a precise temperature stabilization. The temperature changes were measured with a small-bead thermistor glued to the sample; the temperature was measured using a digital multimeter. The EC temperature change (ΔT_{EC}) values presented in this work are the measured maximum temperature changes multiplied by a correction factor of 1.60–1.75, which accounts for the passive part of the sample and also the thermal losses in the gold wires, the silver paste and the thermistor. The used correction factor agrees well with the results of the numerical simulation.[48] The details of the method can be found in ref. 49.

Field-cooled (FC) DC magnetic moment *vs.* temperature was measured between −270 °C and 127 °C at different magnetic fields (0.02–90 kOe) using a physical property measurement system vibrating sample magnetometer (PPMS-VSM, Quantum Design, California, USA). Furthermore, the magnetization–magnetic field (M–H) hysteresis loops were obtained in magnetic fields up to 90 kOe at temperatures of −270 °C and RT. For the measurements rod-like-shaped ceramic samples were used. The M values were obtained by normalizing the magnetic moment values by the mass of the samples. The MC effect was determined by the indirect method,[50] where the MC temperature change (ΔT_{MC}) was calculated from the magnetization *versus* temperature measurements at different magnetic fields (0.5–90 kOe).

III. Results and discussion

A. $(1-x)Pb(Fe_{0.5}Nb_{0.5})O_3–xBiFeO_3$

In the first part, multiferroic properties of PFN–100xBFO (x = 0–0.5) solid solutions were investigated. All prepared ceramics were single-phase, homogeneous and highly dense ($>$97.6% of the crystallographic density), as previously reported in ref. 42. The temperature
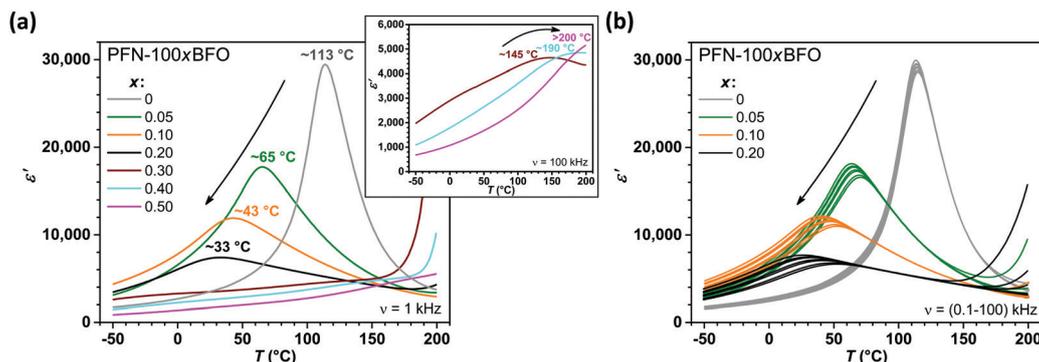
11284 | *J. Mater. Chem. C,* 2020, **8**, 11282–11291

This journal is © The Royal Society of Chemistry 2020

Fig. 1 (a) Temperature dependences of ε' for PFN−100xBFO measured at 1 kHz ($x = 0−0.5$) and (inset) 100 kHz ($x \geq 0.3$). (b) Temperature and frequency dependence of ε' for PFN−100xBFO ($x \leq 0.2$) measured in the frequency range of 0.1–100 kHz.

dependences of the real component of the relative permittivity ε' for all compositions measured at 1 kHz are shown in Fig. 1a. The peak-permittivity of PFN−100xBFO is shifting towards RT with an increasing amount of BFO ($x \leq 0.2$) and it reaches the lowest value in PFN−20BFO, i.e., 33 °C (Fig. 1a). This is accompanied with an increasing relaxor behavior, as seen in Fig. 1b and reported in ref. 42. By further increasing the BFO content ($x \geq 0.3$), the peak-permittivity temperature seemingly shifts to temperatures above the one of PFN (i.e., 113 °C), as visible from ε' measurements at 100 kHz (inset of Fig. 1a). A reason for the progressively increased relaxor behavior by the addition of BFO is most probably related to the increased compositional disorder at the A-site of the perovskite structure, which arises when different multivalence ions occupy a crystalographically equivalent place in the crystal lattice.[42,51,52] Heterovalent substitution of the differently sized Pb^{2+} (119 pm)[53] and Bi^{3+} (103 pm)[53] ions appears to disturb a long-range ferroelectric order in PFN-rich PFN–BFO solid solutions as previously suggested for Pb-based relaxors.[54]

In the next step, the influence of BFO addition on the magnetic properties of PFN−100xBFO was studied. The $M(T)$ curves of all compositions, measured at magnetic field of 1 kOe, are shown in Fig. 2a. In all the samples M increases with the decreasing temperature reaching a maximum value of

∼0.032 emu g^{-1} at −270 °C in PFN. PFN exhibits the paramagnetic-to-antiferromagnetic phase transition (T_N) at −120 °C. With an increase in the amount of BFO, T_N is almost linearly shifted towards higher temperatures reaching RT in PFN−20BFO (Fig. 2b). In PFN−50BFO T_N is probably shifted beyond the measured temperature range (i.e., above 130 °C), which is in agreement with previously reported studies.[55] As demonstrated in Fig. 2b, increasing T_N values with an increasing amount of BFO in PFN–BFO solid solutions are directly related to the higher amount of Fe^{3+} on the B-site perovskite lattice. These results agree well with the previously reported studies, where it was shown that in pure PFN[56] as well as in PFN−50BFO[57,58] the magnetic properties and thus T_N depend on the number of Fe–O–Fe linkages in the structure. Therefore, in our case, the substitution of similarly large Nb^{5+} with Fe^{3+} ions (∼64 pm)[53] increases the Fe/Nb atomic ratio on the B-site sublattice, leading to a higher temperature of the paramagnetic-to-antiferromagnetic phase transition. On the other hand, a decrease in the Nb^{5+} concentration reduces the tendency for the formation of a short-range spin-glass-like phase at low temperatures, which is reflected in lower M values in BFO-rich compared to PFN-rich PFN–BFO solid solutions (Fig. 2a).[25,59] In all compositions slim antiferromagnetic M–H hysteresis loops with almost zero remanent magnetization were obtained at −270 °C (ESI,† C), which
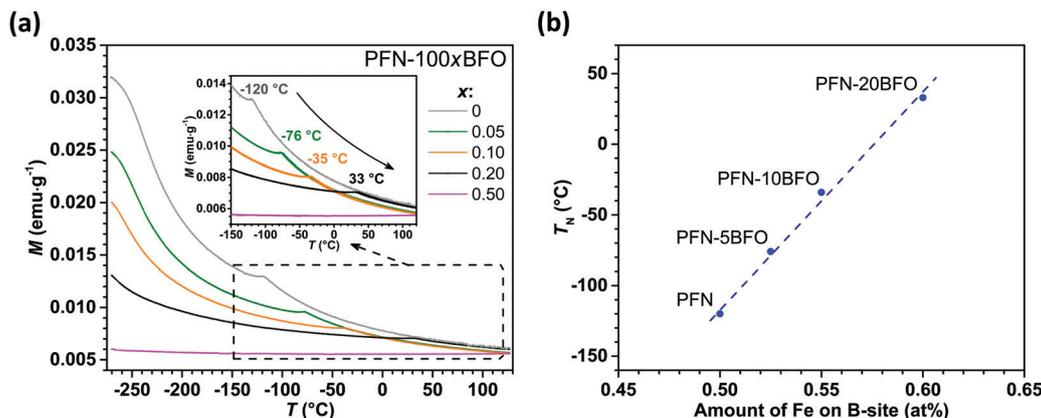

Fig. 2 (a) Temperature dependences of M for PFN−100xBFO ($x = 0−0.5$) measured at 1 kOe. Inset: The enlarged view of the data between −150 °C and 120 °C where T_N is highlighted. (b) Relationship between T_N and the amount of Fe on B-site perovskite sublattice for PFN−100xBFO ($x = 0−0.2$).

indicates that in the PFN–BFO system the increasing BFO content does not significantly affect the long-range antiferromagnetic ordering.

Among all the compositions, PFN–20BFO exhibits the dielectric permittivity anomaly as well as the paramagnetic-to-antiferromagnetic phase transition at RT, which makes this material a promising candidate for room-temperature multicaloric cooling. However, further evaluation of its EC and MC properties revealed some issues, namely excessive electrical conductivity and poor magnetic response, which limit its cooling capability (ESI,† D). At higher temperatures and applied electric fields the increased electrical conductivity leads to the appearance of Joule heating (JH), which significantly reduces material's EC response reaching the maximum EC effective cooling (ΔT_{eff}, defined as the difference between ΔT_{EC} and ΔT_{JH}) of 0.50 °C at RT and 90 kV cm^{-1} (ESI†, D and E). On the other hand, the antiferromagnetic nature of the sample results in a low MC effect over the entire measured temperature range (from −270 to 130 °C) with the maximum value of only 0.07 °C at −270 °C and 50 kOe. Furthermore, despite the vicinity of T_N, no increase in the MC effect at RT in comparison to the previously published PFN[23] was observed (ESI†, D). According to the literature, in PFN and BFO-based materials excessive electrical conductivity and consequently JH can be suppressed by the addition of small amounts of Mn ions,[23,32–34] while the ferromagnetic response can be enhanced by the addition of Gd ions.[36–39] Based on that, in the second part of this study the influence of Mn and Gd doping on the multiferroic and multicaloric properties of PFN–20BFO is discussed.

B. Mn-doped and Gd,Mn co-doped PFN–20BFO

In the second part of this study, the effect of Mn and Gd addition on the structural, microstructural and functional properties of PFO–20BFO was investigated. Firstly, the phase composition, crystal symmetry and microstructure of pure, Mn-doped and Gd,Mn co-doped PFN–20BFO were studied. The X-ray powder diffraction patterns of crushed ceramic pellets are shown in Fig. 3a. In all three samples only the peaks

corresponding to the perovskite phase are present and no additional peaks corresponding to the secondary phases are observed. Rietveld refinement analysis (ESI,† B) revealed that all three compositions exhibit a pseudocubic symmetry at RT ($Pm\bar{3}m$ space group), which is consistent with the previous studies of pure PFN–20BFO.[42,60,61]

The SEM images of the polished sample surfaces are shown in Fig. 3b. All three samples are highly dense, *i.e.*, equal or more than 97.6% of the crystallographic density, exhibiting homogeneous and uniform microstructures. In the microstructure of pure and Mn-doped PFN–20BFO no visible secondary phases are present, while in the Gd,Mn co-doped sample small dark inclusions are observed. A qualitative EDXS analysis revealed that these dark phase regions correspond to Fe-rich and Gd,Nb-rich secondary phases (details in ESI†, F). The average grain sizes of pure and Mn-doped PFN–20BFO are in the range of 1 μm, while the grain size of the Gd,Mn co-doped sample is larger (~4.8 μm) due to the higher sintering temperature. In all three samples, monomodal grain size distribution, indicating the normal grain growth during the sintering, was observed (ESI†, G).

The temperature and frequency (ν) dependence of the real component of relative permittivity ε' and dielectric loss $\tan\delta$ of all three PFN–20BFO-based compositions are shown in Fig. 4. Pure PFN–20BFO exhibits broad and diffusive peak-permittivity with the maximal value of ~7700 at 0.1 kHz and 27 °C indicating relaxor-like behavior (Fig. 4a).[42] The sample shows a large frequency dependence of peak-permittivity temperature ($T_{\varepsilon,max}$) that is spanning from 27 °C at 0.1 kHz to 53 °C at 100 kHz (*i.e.*, $\Delta T_{\varepsilon,max}$ of 26 °C). The addition of 0.5 mol% Mn resulted in slightly lower peak-permittivity values with $T_{\varepsilon,max}$ shifted to higher temperatures, reaching the maximum value of ~6200 at 0.1 kHz and 65 °C (Fig. 4b). While further addition of 12 mol% Gd shifts the $T_{\varepsilon,max}$ to slightly lower temperatures compared to pure PFN–20BFO with the maximum value of ~5800 at 0.1 kHz and 18 °C (Fig. 4c). Both modifications of PFN–20BFO lead to a weakening of the relaxor behavior, which is reflected in smaller $\Delta T_{\varepsilon,max}$, namely ~5 °C in both
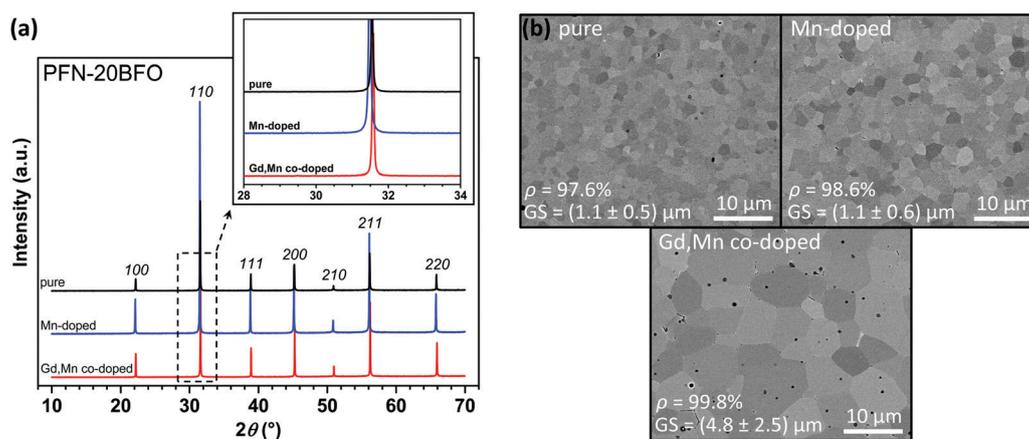

Fig. 3 (a) Room-temperature XRD patterns of PFN–20BFO-based compositions. The indexed peaks of the perovskite phase are labeled according to the cubic notation. The inset shows an enlarged 2θ region from 28° to 34°, where no peaks of secondary phases are observed. (b) SEM micrographs of polished PFN–20BFO-based compositions.
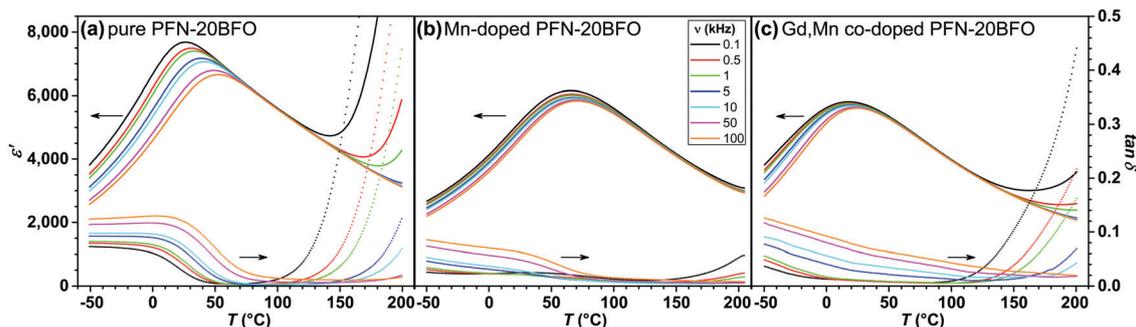
11286 | *J. Mater. Chem. C*, 2020, **8**, 11282–11291

This journal is © The Royal Society of Chemistry 2020

Fig. 4 Temperature and frequency dependences of ε' and $\tan\delta$ of (a) pure, (b) Mn-doped and (c) Gd,Mn co-doped PFN–20BFO.

samples. In all three samples high room-temperature ε' values are observed, ranging from ~ 5200 to ~ 7700 at 0.1 kHz.

The $\tan\delta$ of all three compositions are frequency-dependent with relatively low values at RT, namely from 0.05 to 0.01 at 1 kHz (Fig. 4). Due to the enhanced electrical conductivity in pure PFN–20BFO, above 120 °C the $\tan\delta$ significantly increases. The addition of Mn ions successfully reduces the $\tan\delta$ throughout the entire temperature range showing very low values even at high temperatures, i.e., ~ 0.05 at 200 °C and 0.1 kHz (Fig. 4b). Further modification of the material by Gd ions leads back to an increase in $\tan\delta$, but the values remain comparable or even slightly lower than that in pure PFN–20BFO.

To further investigate the influence of Mn and Gd doping on electrical conductivity, the DC j–E responses of samples were measured at RT (Fig. 5a). As expected, the highest σ_{DC} was obtained in pure PFN–20BFO, namely $\sim 3.0 \times 10^{-10} \ \Omega^{-1} \ m^{-1}$. The addition of 0.5 mol% Mn successfully reduces the electrical conductivity of the material, leading to ~ 20 times lower room-temperature σ_{DC} value, i.e., $\sim 1.7 \times 10^{-11} \ \Omega^{-1} \ m^{-1}$. On the other hand, further addition of Gd does not significantly increase the electrical conductivity at RT, which still remains low and comparable to that of the Mn-doped one (i.e., $\sim 2.0 \times 10^{-11} \ \Omega^{-1} \ m^{-1}$).

The influence of Mn and Gd doping on room-temperature P–E hysteresis loop measurements was investigated (Fig. 5b). Pure PFN–20BFO exhibits relatively slim and tilted relaxor-like P–E hysteresis loops with a coercive electric field (E_C) and saturated polarization (P_S) of ~ 2.8 kV cm^{-1} and ~ 38 μC cm^{-2},

respectively. The results are in agreement with the previous study.[42] The addition of 0.5 mol% Mn does not significantly affect the P–E response, where E_C remains comparable to the one in pure PFN–20BFO, while P_S is slightly lower, i.e., ~ 34 μC cm^{-2}. Further addition of Gd resulted in even slimmer room-temperature hysteresis loops with lower E_C and P_S values, namely ~ 1.5 kV cm^{-1} and ~ 32 μC cm^{-2}, respectively. Note that this is most probably related to the lower peak-permittivity temperature and more pronounced cubic symmetry in this composition at RT (ESI,† B). In addition, both modified compositions exhibit sharp P–E loop ends, indicating low electrical conductivity of the materials even at higher applied electric fields.

As previously demonstrated in PFN[23,62] as well as BFO-based[33,34] ceramics, a reason that such a small amount of Mn successfully suppresses the enhanced electrical conductivity of the material could be related to the nature of the Mn ions, which are known to undergo different oxidation states (for example 4+, 3+ or 2+ in this case) and thus easily compensate possible charge imbalances in the system. Consequently, Mn ions most likely lead to a lower concentration of charge point defects, leading to suppressed electrical conductivity at high temperatures and high electric fields. On the other hand, further addition of Gd does not significantly affect the ferroelectric and dielectric properties of the material, where dilution of ferroelectrically active Bi^{3+} ions by magnetic Gd^{3+} ions causes only a slight shift of $T_{\varepsilon,max}$ towards lower temperatures.

After structural, microstructural and electrical characterization, the influence of Mn and Gd doping on the magnetic properties
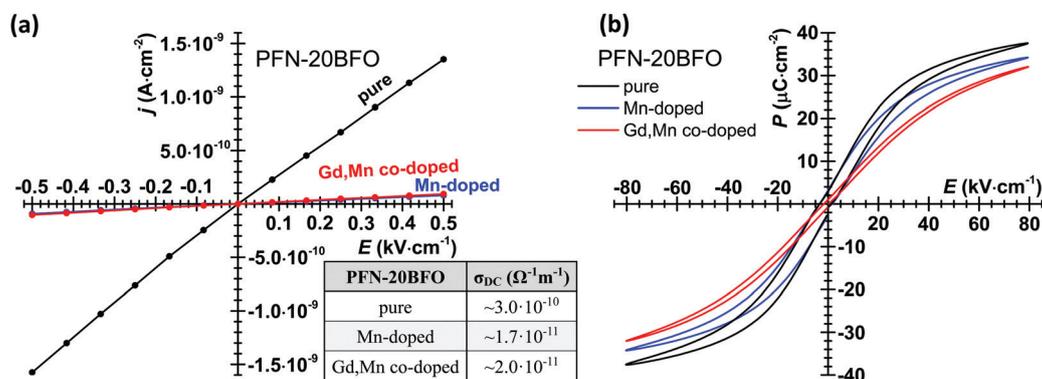

Fig. 5 (a) j–E curves with (inset) related σ_{DC} values and (b) P–E hysteresis loops of PFN–20BFO-based compositions measured at RT.

PFN-20BFO	σ_{DC} ($\Omega^{-1} m^{-1}$)
pure	$\sim 3.0 \cdot 10^{-10}$
Mn-doped	$\sim 1.7 \cdot 10^{-11}$
Gd,Mn co-doped	$\sim 2.0 \cdot 10^{-11}$

This journal is © The Royal Society of Chemistry 2020

J. Mater. Chem. C, 2020, 8, 11282–11291 | 11287

of PFN–20BFO was studied. The $M(T)$ curves of all three PFN–20BFO-based compositions, measured at a magnetic field of 1 kOe, are shown in Fig. 6a. In all three cases an increasing trend of M with a decreasing temperature is observed. Even the addition of only 0.5 mol% Mn ions slightly affects the magnetic properties of the material, where compared to pure PFN–20BFO, $\sim$10% higher magnetization values are obtained over the entire measuring temperature range. As already mentioned, Fe–O–Fe linkages define the magnetic properties in this system.[56–58] The substitution of larger Fe^{3+} ions (64.5 pm, $3d^5$)[53] with smaller Mn^{4+} ions (53 pm, $3d^3$)[53] changes the local structure of FeO_6

octahedra,[63,64] leading to contraction of the lattice parameters (ESI,† B). Consequently, a shorter Mn–O bond and thus different angles of Fe–O–Mn linkages in comparison to the initial Fe–O–Fe lead to a slightly different magnetic arrangement in the structure.[64,65] According to the previous studies, it was found that Fe–O–Mn can slightly distort the long-range antiferromagnetic order, inducing more ferrimagnetic-like spin configuration and thus slightly larger macroscopic magnetization.[66] The same trend, namely slightly increased magnetization in the entire temperature range, was also observed in Mn-doped PFN ceramics.[23]

Further doping with Gd ions results in a significant enhancement of magnetic properties, especially at low temperatures. Compared to pure PFN–20BFO, the Gd,Mn co-doped sample exhibits $\sim$30% larger room-temperature magnetization (inset of Fig. 6a and b). While at lower temperatures more than 11 times higher maximum value of M is obtained, namely $\sim$0.144 emu g^{-1} at −270 °C and 1 kOe. This significantly higher magnetic response of the Gd, Mn co-doped sample is also reflected in M–H hysteresis loop measurements at −270 °C (Fig. 6c). Similarly, a large enhancement of M at low temperatures was also reported for Gd-doped BFO,[36,38,39,67] where such an enhanced magnetic response is described by the alignment of Gd^{3+} and Fe–O–Fe magnetic moments in the same direction. At low temperatures, paramagnetic Gd^{3+} ions (partially filled seven 5f-orbitals) that possess high magnetic moments align with the antiferromagnetic Fe–O–Fe subsystem (f–d exchange orbital interaction), leading to significant enhancement of magnetization.[36,67,68] This contribution is less pronounced at higher temperatures, which is reflected in lower magnetization values.

As seen above, the addition of Mn and Gd enhances the magnetic properties of PFN–20BFO but at the same time, it does not influence its relaxor behavior that remains comparable to that of pure PFN–20BFO. Even more, both modified compositions exhibit relaxor-like hysteresis loops with sharp ends indicating low electrical conductivity even at higher applied electric fields, which make them promising candidates for multicalorics. Therefore, in the next step, the EC and MC effects of Mn and Gd,Mn modified compositions were studied.

The temperature dependence of ΔT_{EC} at different applied electric fields for Mn-doped PFN–20BFO is shown in Fig. 7a. The addition of 0.5 mol% Mn reduces the electrical conductivity, which enables the measurements of EC effects at higher temperatures and applied electric fields compared to pure PFN–20BFO (see Fig. S5a (ESI†) and compare with Fig. 7a). Mn-doped PFN–20BFO exhibits a high room-temperature ΔT_{EC} value of $\sim$1.5 °C at 150 kV cm^{-1}, which is comparable to that of previously studied Mn-doped PFN.[23] By increasing the temperature, ΔT_{EC} increases and reaches the maximum value of $\sim$1.8 °C at 76 °C and 150 kV cm^{-1} (Fig. 7a). Additional doping with Gd resulted in a slightly lower ΔT_{EC}, namely $\sim$1.13 °C at RT and 140 kV cm^{-1}. As seen in Fig. 4c, the peak-permittivity temperature of the Gd,Mn co-doped sample is below RT. As the temperature increases, no additional anomalies are observed, resulting in a nearly constant ΔT_{EC} of 1.15 °C ± 0.02 °C.

In Mn-doped PFN–20BFO at temperatures below 70 °C almost negligible JH ($<$3%) is present, resulting in a good
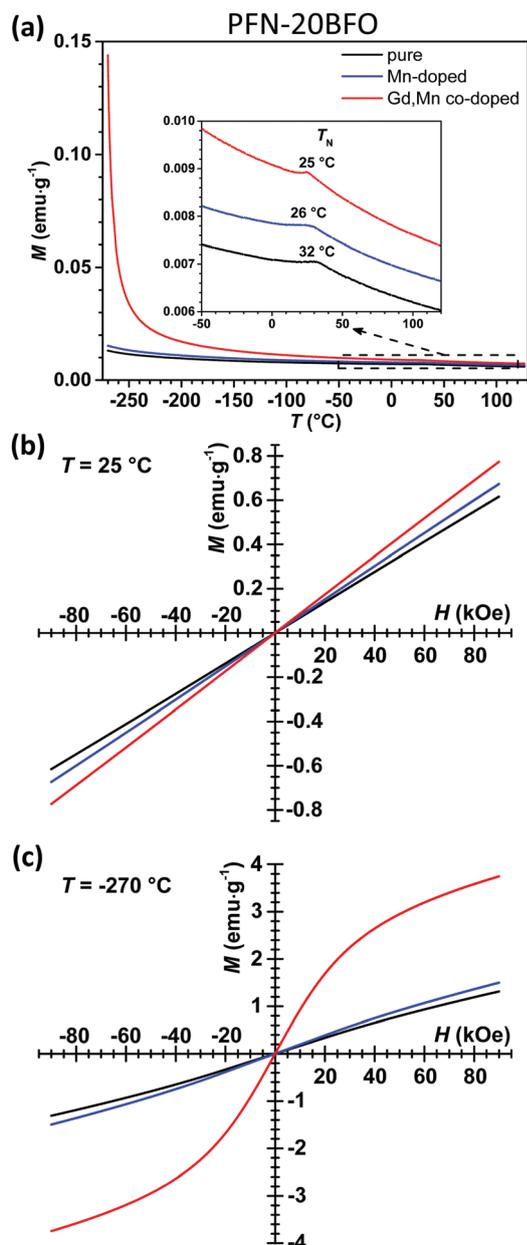

Fig. 6 (a) Temperature dependences of M for PFN–20BFO-based composition measured at 1 kOe. Inset: The enlarged view of the data between −50 °C and 120 °C where T_N is highlighted. M–H hysteresis loops of PFN–20BFO-based compositions measured at (b) RT and (c) −270 °C.
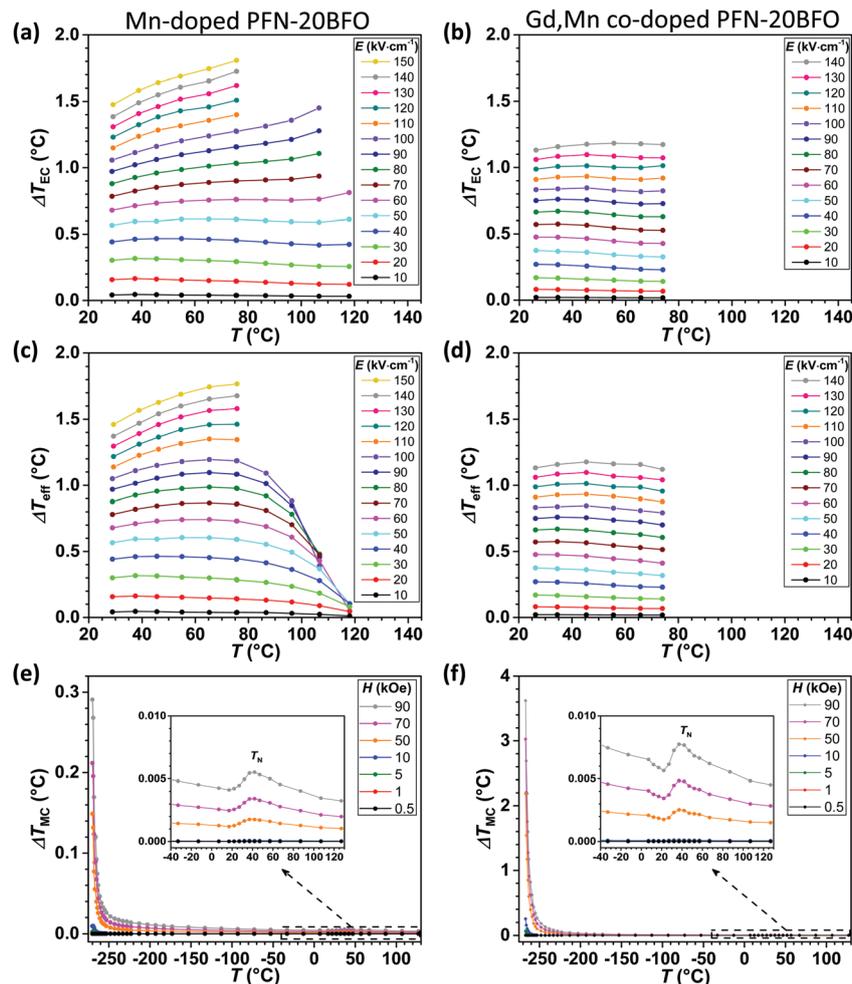
11288 | J. Mater. Chem. C, 2020, 8, 11282–11291

This journal is © The Royal Society of Chemistry 2020

Fig. 7 Multicaloric properties of (a,c and e) Mn-doped and (b,d and f) Gd,Mn co-doped PFN–20BFO; (a and b) ΔT_{EC} and (c and d) ΔT_{eff} measured at different temperatures and applied electric fields. Due to the constant trend, EC measurements of the Gd,Mn co-doped sample were performed only up to 75 °C. (e and f) ΔT_{MC} measured at different temperatures and applied magnetic field with the inset showing an enlarged view of the data between −40 °C and 130 °C. Note the differences in scales of ΔT_{MC}. Lines between the measured values are just a guide to the eye.

match of ΔT_{eff} with the ΔT_{EC} values (Fig. 7c). Above 80 °C, the JH starts to increase, causing a gradual lowering of the effective EC cooling effect. Negligible JH ($<5\%$) was also observed in the Gd,Mn co-doped sample, where ΔT_{eff} remains more or less identical to ΔT_{EC} until 75 °C (Fig. 7d).

The temperature dependences of ΔT_{MC} (calculated from $M(T)$ curves shown in ESI†, C) at different applied magnetic fields for Mn-doped and Gd,Mn co-doped PFN–20BFO are shown in Fig. 7e and f, respectively. A slight improvement in the magnetization of the Mn-doped sample in comparison to pure PFN–20BFO (see Fig. 6a) is also reflected in the MC effect, where ∼20% higher room-temperature ΔT_{MC} is observed. However, at low temperatures ∼2 times higher ΔT_{MC} of ∼0.15 °C at −270 °C and 50 kOe is obtained (insets of Fig. 7e). In agreement with enhanced magnetic properties, further addition of Gd ions causes a significant improvement of the MC effect over the entire temperature range, resulting in ∼65% higher ΔT_{MC} at RT and more than 30 times higher ΔT_{MC} at −270 °C (∼2.2 °C at 50 kOe) compared to pure PFN–20BFO (Fig. 7f). Furthermore, in this

material room-temperature ΔT_{MC} ∼8×10^{-3} °C is obtained at 90 kOe, which is so far the highest value among the PFN-based multicalorics.[22,23,69] On the other hand, the sample exhibits an extremely high ΔT_{MC} value of 3.6 °C at −270 °C and 90 kOe. Considering that this is an indirect measurement and that temperature of −273.15 °C (0 K) cannot be reached, we estimate that the ΔT_{MC} value is below 3 °C.

IV. Summary and conclusions

In this work, a series of single-phase PFN–100xBFO solid solutions (x = 0–0.5) were prepared by mechanochemical synthesis followed by sintering. The influence of BFO addition on the temperatures of magnetic susceptibility and dielectric permittivity anomalies was studied. With an increase in the amount of BFO, the paramagnetic–antiferromagnetic phase transition of PFN–BFO shifts toward higher temperatures, while the peak-permittivity temperature first decreases (to RT when x = 0.2) and then increases to higher temperatures (in $x > 0.2$ compositions). The dielectric

This journal is © The Royal Society of Chemistry 2020

J. Mater. Chem. C, 2020, **8**, 11282–11291 | **11289**

Table 1 Summary of room-temperature and maximum (a) EC and (b) MC effect values for PFN–20BFO-based compositions

(a)	Sample	T (°C)	E (kV cm^{-1})	ΔT_{eff} (°C)
EC effect	Pure	RT	90	0.50
	Mn-doped	RT	90	0.97
			150	1.5
		$T_{\text{EC,max}}$ (76 °C)	150	1.8
	Gd,Mn co-doped	RT	90	0.75
			140	1.1

(b)	Sample	T (°C)	H (kOe)	ΔT_{MC} (°C)
MC effect	Pure	RT	50	0.0015
		$T_{\text{MC,max}}$ (−270 °C)	50	0.07
	Mn-doped	RT	50	0.0018
		$T_{\text{MC,max}}$ (−270 °C)	50	0.15
	Gd,Mn co-doped	RT	50	0.0025
		$T_{\text{MC,max}}$ (−270 °C)	50	2.2

permittivity and magnetic susceptibility anomalies coincide at RT in PFN–20BFO composition, making it a promising candidate for multicaloric applications. However, due to the excessive Joule heating and its antiferromagnetic nature, PFN–20BFO exhibits low EC and MC effects in the entire measuring temperature range with the maximum values of 0.50 °C (at RT and 90 kV cm^{-1}) and 0.07 °C (at −270 °C and 50 kOe), respectively (Table 1). Therefore, the EC and MC properties of PFN–20BFO were further improved by doping with Mn and Gd ions.

The addition of 0.5 mol% Mn successfully suppresses the electrical conductivity and consequently the Joule heating effect in the material, which resulted in a high room-temperature EC effect of 1.5 °C, and even a higher maximum value of 1.8 °C at 76 °C (Table 1a). At the same time, the addition of Mn also slightly improves the MC properties of the material, resulting in ~20% higher room-temperature and ~2 times higher maximum ΔT_{MC} compared to pure PFN–20BFO (Table 1b). Further addition of 12 mol% Gd leads to a significant enhancement of the MC effect in the entire measurement temperature range, exhibiting ~65% higher room-temperature and more than 30 times higher maximum ΔT_{MC} compared to pure PFN–20BFO (Table 1b). At the same time, the room-temperature electrical conductivity remains comparable to that of Mn-doped PFN–20BFO, which resulted in negligible Joule heating and EC effects of more than one degree over a wide temperature range.

Despite the fact that in the prepared PFN–20BFO-based materials both ferroic anomalies are located at RT, the maximum MC and EC effects are located in two different temperature regions. The use of such multicaloric materials could be in applications where the operating temperature is significantly changing, for example in deep space and extreme measurement under liquid-helium temperature conditions. Further research in this area is needed to prepare better room-temperature single-phase multicalorics that can be used as cooling elements in future solid-state cooling devices for everyday use.

Conflicts of interest

There are no conflicts to declare.

References

1 W. Eerenstein, N. D. Mathur and J. F. Scott, *Nature*, 2006, **442**, 759–765.
2 M. Fiebig, T. Lottermoser, D. Meier and M. Trassin, *Nat. Rev. Mater.*, 2016, **1**, 16046.
3 N. A. Spaldin and R. Ramesh, *Nat. Mater.*, 2019, **18**, 203–212.
4 P. Chandra, *Nat. Mater.*, 2019, **18**, 197–198.
5 N. A. Hill, *J. Phys. Chem. B*, 2000, **104**, 6694–6709.
6 I. Takeuchi and K. Sandeman, *Phys. Today*, 2015, **68**, 48–54.
7 J. Shi, D. Han, Z. Li, L. Yang, S.-G. Lu, Z. Zhong, J. Chen, Q. M. Zhang and X. Qian, *Joule*, 2019, **3**, 1–26.
8 S. Fahler and V. K. Pecharsky, *MRS Bull.*, 2018, **43**, 264–268.
9 L. Manosa, A. Planes and M. Acet, *J. Mater. Chem. A*, 2013, **1**, 4925–4936.
10 S. Fahler, U. K. Rossler, O. Kasther, J. Eckert, G. Eggeler, H. Emmerich, P. Entel, S. Muller, E. Quandt and K. Albe, *Adv. Eng. Mater.*, 2012, **14**, 10–19.
11 X. Moya, S. Kar-Narayan and N. D. Mathur, *Nat. Mater.*, 2014, **13**, 439–450.
12 M. M. Vopson, *Crit. Rev. Solid State Mater. Sci.*, 2015, **40**, 223–250.
13 M. M. Vopson, *Solid State Commun.*, 2012, **152**, 2067–2070.
14 E. Stern-Taulats, T. Castan, L. Manosa, A. Planes, N. D. Mathur and X. Moya, *MRS Bull.*, 2018, **43**, 295–299.
15 B. Rozic, M. Kosec, H. Ursic, J. Holc, B. Malic, Q. M. Zhang, R. Blinc, R. Pirc and Z. Kutnjak, *J. Appl. Phys.*, 2011, **110**, 064118.
16 M. M. Vopson, *J. Phys. D: Appl. Phys.*, 2013, **46**, 345304.
17 H. Meng, B. Li, W. Ren and Z. Zhang, *Phys. Lett. A*, 2013, **377**, 567–571.
18 A. Planes, T. Castan and A. Saxena, *Philos. Mag.*, 2014, **94**, 1893–1908.
19 A. Kumar and K. L. Yadav, *J. Appl. Phys.*, 2014, **116**, 083907.
20 A. S. Starkov and I. A. Starkov, *J. Exp. Theor. Phys.*, 2014, **119**, 258–263.
21 J. Krishna Murthy and A. Venimadhav, *J. Phys. D: Appl. Phys.*, 2014, **47**, 445002.
22 H. Ursic, V. Bobnar, B. Malic, C. Filipic, M. Vrabelj, S. Drnovsek, Y. Jo, M. Wencka and Z. Kutnjak, *Sci. Rep.*, 2016, **6**, 26629.
23 U. Prah, T. Rojac, M. Wencka, M. Dragomir, A. Bradesko, A. Bencan, R. Sherbondy, G. Brennecka, Z. Kutnjak, B. Malic and H. Ursic, *J. Eur. Ceram. Soc.*, 2019, **39**, 4122–4130.
24 M. Yokosuka, *Jpn. J. Appl. Phys.*, 1993, **32**, 1142–1146.

11290 | *J. Mater. Chem. C*, 2020, **8**, 11282–11291

This journal is © The Royal Society of Chemistry 2020

25 V. V. Laguta, J. Rosa, L. Jastrabik, R. Blinc, P. Cevc, B. Zalar, M. Remskar, S. I. Raevskaya and I. P. Raevski, *Mater. Res. Bull.*, 2010, **45**, 1720–1727.

26 A. Kumar, R. S. Katiyar, C. Rinaldi, S. G. Lushnikov and T. A. Shaplygina, *Appl. Phys. Lett.*, 2008, **93**, 232902.

27 G. Catalan and J. F. Scott, *Adv. Mater.*, 2009, **21**, 2463–2485.

28 T. Rojac, A. Bencan, B. Malic, G. Tutuncu, J. L. Jones, J. E. Daniels and D. Damjanovic, *J. Am. Ceram. Soc.*, 2014, **97**, 1993–2011.

29 A. Bradesko, A. Hedl, L. Fulanovic, N. Novak and T. Rojac, *APL Mater.*, 2019, **7**, 071111.

30 M. Quintero, L. Ghivelder, F. Gomez-Marlasca and F. Parisi, *Appl. Phys. Lett.*, 2011, **99**, 232908.

31 M. Quintero, P. Gaztanaga and I. Irurzun, *Appl. Phys. Lett.*, 2015, **107**, 151901.

32 D. Bochenek and P. Guzdek, *J. Magn. Magn. Mater.*, 2011, **323**, 369–374.

33 M. Makarovic, J. Walker, E. Khomyakova, A. Bencan, B. Malic and T. Rojac, *Informacije MIDEM*, 2016, **46**, 154–159.

34 S. O. Leontsev and R. E. Eitel, *J. Am. Ceram. Soc.*, 2009, **92**, 2957–2961.

35 G. L. Yuan, S. W. Or, Y. P. Wang, Z. G. Liu and J. M. Liu, *Solid State Commun.*, 2006, **138**, 76–81.

36 V. A. Khomchenko, V. V. Shvartsman, P. Borisov, W. Kleemann, D. A. Kiselev, I. K. Bdikin, J. M. Vieira and A. L. Kholkin, *Acta Mater.*, 2009, **57**, 5137–5145.

37 J. Walker, H. Ursic, A. Bencan, B. Malic, H. Simons, I. Reaney, G. Viola, V. Nagarajan and T. Rojac, *J. Mater. Chem. C*, 2016, **4**, 7859–7868.

38 V. Sobol, B. Korzun, O. Mazurenko, T. Bizhigitov and S. Tomaev, *MRS Adv.*, 2019, **4**, 1989–1999.

39 D. Lukovic Golic, A. Radojkovic, A. Dapcevic, D. Pajic, J. Dragovic, F. Toric, J. Cirkovic, G. Brankovic and Z. Brankovic, *Ceram. Int.*, 2019, **45**, 19158–19165.

40 J. J. Rhyne and T. R. McGuire, *IEEE Trans. Magn.*, 1972, **8**, 105–130.

41 S. Karimi, I. M. Reaney, Y. Han, J. Pokorny and I. Sterianou, *J. Mater. Sci.*, 2009, **44**, 5102–5112.

42 U. Prah, M. Dragomir, T. Rojac, A. Bencan, R. Broughton, C.-C. Chung, J. L. Jones, R. Sherbondy, G. Brennecka and H. Ursic, *J. Mater. Chem. C*, 2020, **8**, 3452–3462.

43 D. Kuscer, T. Bakaric, B. Kozlevcar and M. Kosec, *J. Phys. Chem. B*, 2013, **117**, 1651–1659.

44 J. Walker, P. Bryant, V. Kurusingal, C. Sorrell, D. Kuscer, G. Drazic, A. Bencan, V. Nagarajan and T. Rojac, *Acta Mater.*, 2015, **83**, 149–159.

45 R. Font, O. Raymond-Herrera, L. Mestres, J. Portelles, J. Fuentes and J. M. Siqueiros, *J. Mater. Sci.*, 2016, **51**, 6319–6330.

46 D. Wilcox, B. Dove, B. McDavid and D. Greer, *UTHSCSA Image Tool for Windows Version 3.0.*, University of Texas Health Science Center, San Antonio, TX, 2002.

47 W. H. Walton, *Nature*, 1948, **162**, 329–330.

48 A. Bradesko, L. Fulanovic, M. Vrabelj, M. Otonicar, H. Ursic, A. Henriques, C.-C. Chung, J. L. Jones, B. Malic, Z. Kutnjak and T. Rojac, *Acta Mater.*, 2019, **169**, 275–283.

49 Z. Kutnjak and B. Rožič, Indirect and Direct Measurements of the Electrocaloric Effect, in *Electrocaloric Materials. New Generation of Coolers*, ed. T. Correia and Q. Zhang, Springer, Berlin, Heidelberg, 2014, vol. 147.

50 A. M. Tishin and Y. I. Spichkin, *The Magnetocaloric Effect and its Applications*, Institute of Physics Publishing, Bristol, UK, 2003.

51 A. A. Bokov and Z.-G. Ye, *J. Mater. Sci.*, 2006, **41**, 31–52.

52 F. Li, S. Zhang, D. Damjanovic, L.-Q. Chen and T. R. Shrout, *Adv. Funct. Mater.*, 2018, **28**, 1801504.

53 R. D. Shannon, *Acta Crystallogr., Sect. A: Cryst. Phys., Diffr., Theor. Gen. Crystallogr.*, 1976, **32**, 751–767.

54 F. Chu, I. M. Reaney and N. Setter, *J. Appl. Phys.*, 1995, **77**, 1671–1676.

55 G. A. Smolenskii and V. M. Yudin, *Phys. Solid State*, 1965, **6**, 2936–2942.

56 V. V. Bhat, K. V. Ramanujachary, S. E. Lofland and A. M. Umarji, *J. Magn. Magn. Mater.*, 2004, **280**, 221–226.

57 A. Stoch, J. Maurin, J. Kulawik and P. Stoch, *J. Eur. Ceram. Soc.*, 2017, **37**, 1467–1476.

58 A. Stoch and P. Stoch, *Ceram. Int.*, 2018, **44**, 14136–14144.

59 S. Chillal, M. Thede, F. J. Litterst, S. N. Gvasaliya, T. A. Shaplygina, S. G. Lushnikov and A. Zheludev, *Phys. Rev. B: Condens. Matter Mater. Phys.*, 2013, **87**, 220403.

60 N. N. Krainik, N. P. Khuchua, A. A. Berezhnoi and A. G. Tutov, *Phys. Solid State*, 1965, **7**, 100–107.

61 L. A. Shilkina, A. V. Pavlenko, L. A. Reznitchenko and I. A. Verbenko, *Crystallogr. Rep.*, 2016, **61**, 263–269.

62 B. Fang, Y. Shan and H. Imoto, *Jpn. J. Appl. Phys.*, 2004, **43**, 2568–2571.

63 L. Chen, L. Zheng, Y. He, J. Zhang, Z. Mao and X. Chen, *J. Alloys Compd.*, 2015, **633**, 216–219.

64 Y. Zhang, Y. Wang, J. Qi, Y. Tian, M. Sun, J. Zhang, T. Hu, M. Wei, Y. Liu and J. Yang, *Nanomaterials*, 2018, **8**, 711.

65 I. Sosnowska, W. Schäfer, W. Kockelmann, K. H. Andersen and I. O. Troyanchuk, *Appl. Phys. A: Mater. Sci. Process.*, 2002, **74**, 1040–1042.

66 H. Naganuma, J. Miura and S. Okamura, *Appl. Phys. Lett.*, 2008, **93**, 052901.

67 A. I. Iorgu, F. Maxim, C. Matei, L. P. Ferreira, P. Ferreira, M. M. Cruz and D. Berger, *J. Alloys Compd.*, 2015, **629**, 62–68.

68 I. I. Makoed and A. F. Revinskii, *Phys. Solid State*, 2015, **57**, 1787–1792.

69 U. Prah, M. Wencka, Z. Kutnjak, M. Vrabelj, S. Drnovsek, B. Malic and H. Ursic, *Informacije MIDEM*, 2017, **47**, 165–170.

This journal is © The Royal Society of Chemistry 2020

J. Mater. Chem. C, 2020, **8**, 11282–11291 | 11291